Journal of Energy Chemistry 40 (2020) 15–21

Contents lists available at ScienceDirect

Journal of Energy Chemistry

journal homepage: www.elsevier.com/locate/jechem

http://www.journals.elsevier.com/journal-of-energy-chemistry/

3D porous V_2O_5 architectures for high-rate lithium storage

Qifei Li[a,1], Dong Chen[a,1], Huiteng Tan[a,1], Xianghua Zhang[a], Xianhong Rui[a,b,c,*], Yan Yu[b,d,e,*]

[a] Guangzhou Key Laboratory of Low-Dimensional Materials and Energy Storage Devices, Collaborative Innovation Center of Advanced Energy Materials, School of Materials and Energy, Guangdong University of Technology, Guangzhou 510006, Guangdong, China
[b] Hefei National Laboratory for Physical Sciences at the Microscale, Department of Materials Science and Engineering, Key Laboratory of Materials for Energy Conversion, Chinese Academy of Sciences (CAS), University of Science and Technology of China, Hefei 230026, Anhui, China
[c] State Key Laboratory of Vanadium and Titanium Resources Comprehensive Utilization, Panzhihua 617000, Sichuan, China
[d] Dalian National Laboratory for Clean Energy (DNL), Chinese Academy of Sciences, Dalian 116023, Liaoning, China
[e] State Key Laboratory of Fire Science, University of Science and Technology of China, Hefei 230026, Anhui, China

ARTICLE INFO

Article history:
Received 21 January 2019
Revised 19 February 2019
Accepted 20 February 2019
Available online 1 March 2019

Keywords:
Lithium storage
V_2O_5 cathode
Porous structure
Mass production
High rate

ABSTRACT

The discovery of novel electrode materials promises to unleash a number of technological advances in lithium-ion batteries. V_2O_5 is recognized as a high-performance cathode that capitalizes on the rich redox chemistry of vanadium to store lithium. To unlock the full potential of V_2O_5, nanotechnology solution and rational electrode design are used to imbue V_2O_5 with high energy and power density by addressing some of their intrinsic disadvantages in macroscopic crystal form. Here, we demonstrate a facile and environmental-friendly method to prepare nanorods-constructed 3D porous V_2O_5 architectures (3D-V_2O_5) in large-scale. The 3D porous architecture is found to be responsible for the enhanced charge transfer kinetics and Li-ion diffusion rate of the 3D-V_2O_5 electrode. As the result, the 3D-V_2O_5 surpasses the conventional bulk V_2O_5 by showing enhanced discharge capacity and rate capability (delivering 154 and 127 mAh g^{-1} at 15 and 20 C, respectively).

1. Introduction

Lithium-ion batteries (LIBs) are a popular form of sustainable technology that have made their presence felt in renewable energies industry. As the application of LIBs moving from portable consumer electronics to hybrid electric vehicles, ongoing research has been focusing on the investigation of promising electrode materials to achieve high-performance LIBs for more stringent requirements [1–9]. V_2O_5 that outperforms most of the conventional cathodes (e.g., $LiCoO_2$, $LiFePO_4$, and $LiNiO_2$) satiates the increasing energy demands of LIBs [10–12]. Its exceptionally high specific capacity of 294 mAh g^{-1} (voltage window: 2.0–4.0 V) is endowed by the rich chemistry of V_2O_5 to access plentiful redox reactions via the movement of ions along the layered structure of V_2O_5 [13–18]. Although the thermodynamic expression signifies the available energy depends on the types of electrode materials, the theoretical value of chemical energy being stored in V_2O_5 is difficult to be fully claimed due to the limitation in ion diffusion kinetics and electronic conductivity of V_2O_5. In spite of having such robust intercalation tunnels and ability for multi-electron transition, the realization of a V_2O_5 electrode with high power density requires the optimization of dimensional and transport parameters to overcome the complicated physicochemical reaction environment including the ion diffusion towards the electrode and charge transfer at the electrode/electrolyte interfaces, which is also a puzzle researchers are now trying to solve.

Nanotechnology solution has been used to compensate the intrinsic disadvantages of cathode materials by shortening the ion diffusion time tremendously. Numerous V_2O_5 nanostructures, including nanoparticles, nanowires, nanobelts, nanosheets, nanoflower and etc., have been studied to investigate the significance of nanoscopic architectures towards their electrochemical performances [19–24]. However, it is found that their influence in boosting the power density is still very limited. Thus, researchers are working through this challenge by using rational electrode design to optimize the transportation rate and penetration of electrolyte ion. Designing 3D porous structure is a new wave of research that could be the answer to achieving V_2O_5 cathode with high energy and power density, which makes use of its structural uniqueness to maximize the accessibility and permeability of the electrolyte ion to the active surface beyond the surface region through the porous network [25–29]. Different

* Corresponding authors at: Guangdong University of Technology, Guangzhou 510006, Guangdong, China, and University of Science and Technology of China, Hefei 230026, Anhui, China.
E-mail addresses: xhrui@gdut.edu.cn (X. Rui), yanyumse@ustc.edu.cn (Y. Yu).
[1] These authors contributed equally to this work.

https://doi.org/10.1016/j.jechem.2019.02.010

from the packed materials, porous structure allows the "dead mass" beneath the surface region to be utilized and the electrolyte ions can be replenished in a faster rate. It has also been demonstrated that 3D porous architecture can provide interconnected network for efficient Li^+ transport across the entire structure. In addition, the interconnected network infuses higher mechanical robustness to cope with the volume expansion of the active materials while retaining dimensional stability at the electrode level. Some successful examples have demonstrated the feasibility of this approach. For example, template-directed synthesis has been used to prepare ordered mesoporous electrode [30–32], hydrothermal/solvothermal reaction was attempted to synthesize self-assembled 3D porous structures [33–35], and bio-derived method was reported to construct 3D foam [36].

Given the previous success made in 3D porous V_2O_5 electrode, a question naturally arises: How to put it into real practice? An environmentally friendly, safe and reliable synthesis method is hence a necessity to scale up the production for industrial-scale application. In this paper, we present a facile sol-gel method followed by subsequent annealing step to prepare 3D porous architectures constructed by interconnected V_2O_5 nanorods (abbreviated as 3D-V_2O_5) in large-scale. The 3D porous structures show improved charge transfer kinetics and Li-ion diffusion rate compared to the bulk V_2O_5, giving rise to enhanced lithium storage properties. The successful development of such industry feasible method for mass production of 3D porous V_2O_5 electrode is a good indication for its commercialization in years to come.

2. Experimental

2.1. Synthesis of 3D-V_2O_5

The 3D-V_2O_5 was prepared by a facile sol-gel approach combined with a heat treatment procedure. In a typical synthesis, 28 g oxalic acid ($H_2C_2O_4{\cdot}2H_2O$) was initially dissolved into 220 mL deionized water under vigorous string (1.0 M). Afterward, 10 g V_2O_5 powder was added to the above solution under vigorous stirring at 80 °C until a dark blue solution was formed. Then, the solution was kept stirring at 80 °C for 5 h, and dried in an oven at 80 °C for 12 h. Subsequently, the obtained gels were grounded and annealed at 500 °C under air atmosphere for 5 h. Finally, the 3D-V_2O_5 product with a high yield of ~10 g was obtained.

2.2. Materials characterization

X-ray powder diffraction (XRD) was recorded on a Bruker AXS D8 advance X-ray diffractometer using Cu *Kα* radiation. The morphology was investigated by using a field-emission scanning electron microscopy (FESEM) system (JEOL, Model JSM-7600F), and the nanostructure was characterized by using a transmission electron microscopy (TEM) system (JEOL, Model JEM-2100) operating at 200 kV. The X-ray photoelectron spectroscopy (XPS, Thermo Fisher, Model ESCALAB 250Xi) was used to verify the valence state of vanadium.

2.3. Electrochemical measurements

The coin-type cells were assembled in an argon-filled glovebox, where both moisture and oxygen levels were less than 1 ppm. The cathodes were fabricated by mixing 3D-V_2O_5, carbon black and poly(vinyldifluoride) (PVDF) at a weight ratio of 80:10:10 in n-methyl-2-pyrrolidone (NMP) solvent. The resulting mixture was then pasted onto the aluminium foil and punched into small disks ($Ø = 14$ mm). Lithium foils were used as anodes and the electrolyte solution was made of 1 M $LiPF_6$ in ethylene carbonate (EC)/dimethyl carbonate (DMC) (1/1, w/w). The cells were tested on a NEWARE multi-channel battery test system with galvanostatic charge and discharge in the voltage range of 4.0–2.0 V.

3. Results and discussion

To demonstrate the large-scale synthesis, ~10 g product of the 3D-V_2O_5 was fabricated in this paper (Fig. 1(a)), which is unachievable for V_2O_5 nanomaterials obtained by traditionally hydrothermal and solvothermal methods (generally less than 500 mg) [37–39]. Its crystallographic structure was characterized by X-ray diffraction (XRD) and the corresponding pattern is displayed in Fig. 1(b). The diffraction peaks can be indexed as the orthorhombic V_2O_5 (space group: *Pmmn*(59), JCPDS card no. 41-1426), and there are no impurity peaks. The details on the structure of 3D-V_2O_5 were further examined by Rietveld refinement with the standard orthorhombic structure using TOPAS software. The calculated profile fits well with the measured pattern, and the refinement results indicate that two key factors R_p (profile factor) and R_{wp} (weighted profile factor) are below 15%, showing acceptable values of 10.4% and 12.3%, respectively, and lattice parameters are calculated as $a = 11.50920$ Å, $b = 3.56415$ Å and $c = 4.37649$ Å.

Figs. 2(a) and S1 show low magnification scanning electron microscopy (SEM) images of the 3D-V_2O_5. Large porous clusters with the size of around 10–15 μm (length) × 10 μm (width) are distinguished. With a close-up observation (Fig. 2(b)), the cluster is constructed by interconnected V_2O_5 nanorods (100–500 nm in length), leaving a network of continuous pores. The transmission electron microscopy (TEM) image depicted in Fig. 2(c) indicates that V_2O_5 nanorods are tightly adhered together to form 3D stable architectures. The Selected area electron diffraction (SAED) pattern shown in the inset of Fig. 2(c) can be identified as orthorhombic V_2O_5 on a [001] zone axis. Clear lattice fringes can be seen running parallel to the edge of the nanorod in Fig. 2(d). The spacing was calculated to be 0.35 nm, which corresponds to the (201) plane of orthorhombic V_2O_5 (inset of Fig. 2(d)). It is worth noting that there are significant effects of oxalic acid concentration to preserve the rod-like morphology and porous structure of the 3D-V_2O_5. As illustrated in Fig. S2, the well-defined rod-like morphology diminishes when large amount of oxalic acid (2.0 M) was used and results in a mixture of nanorods and nanoparticles, losing the original uniformity. The structure of the nanorods is retained at a low concentration of oxalic acid (0.1 M), despite a slight difference in the compactness is observed. As illustrated in Fig. S3, the interstitial pore space between the nanorods almost disappears. Such variation in surface morphology is due to the reduced amount of gaseous products formed during calcination. Without the massive gas evolution, volume shrinkage is pronounced and the nanorods are packed densely to reduce the surface energy at high annealing temperature. As a comparative study, bulk V_2O_5 sample was also prepared (i.e., annealing of commercial V_2O_5 at 500 °C in air for 5 h), and its characterization is shown in Fig. S4. Contrarily to the 3D-V_2O_5, the bulk V_2O_5 only shows micron-sized agglomerates, featuring the large solid cluster instead of 3D porous architecture.

Electrochemical properties of the 3D-V_2O_5 were tested in 2032-type coin cells using metallic lithium as the counter electrode at 298 K. Fig. 3(a) shows the initial lithium intercalation/deintercalation curve and the subsequent two discharge/charge profiles under the galvanostatic condition of 0.5 C (147 mA g^{-1}) current density. Obviously, there are three relatively long discharge and charge plateaus, corresponding to a series of two-phase transitions. The plateaus located at 3.4 and 3.2 V correspond to one lithium insertion/extraction ($V_2O_5 \leftrightarrow Li_{0.5}V_2O_5 \leftrightarrow Li_{1.0}V_2O_5$), while 2.3 V (discharge)/2.5 V (charge) is related to another lithium electrochemical reaction ($Li_{1.0}V_2O_5 \leftrightarrow Li_{2.0}V_2O_5$). These lithiation/de-lithiation activities are highly reversible,

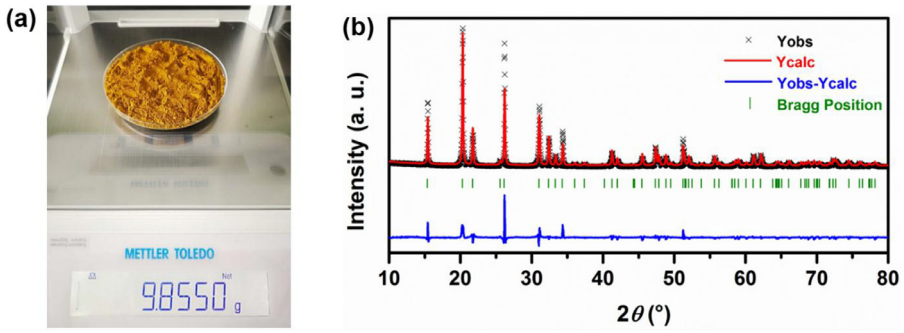

Fig. 1. (a) Digital photograph of the as-prepared 3D-V_2O_5 with a weight of ~10 g. (b) Rietveld refined XRD pattern of the 3D-V_2O_5.

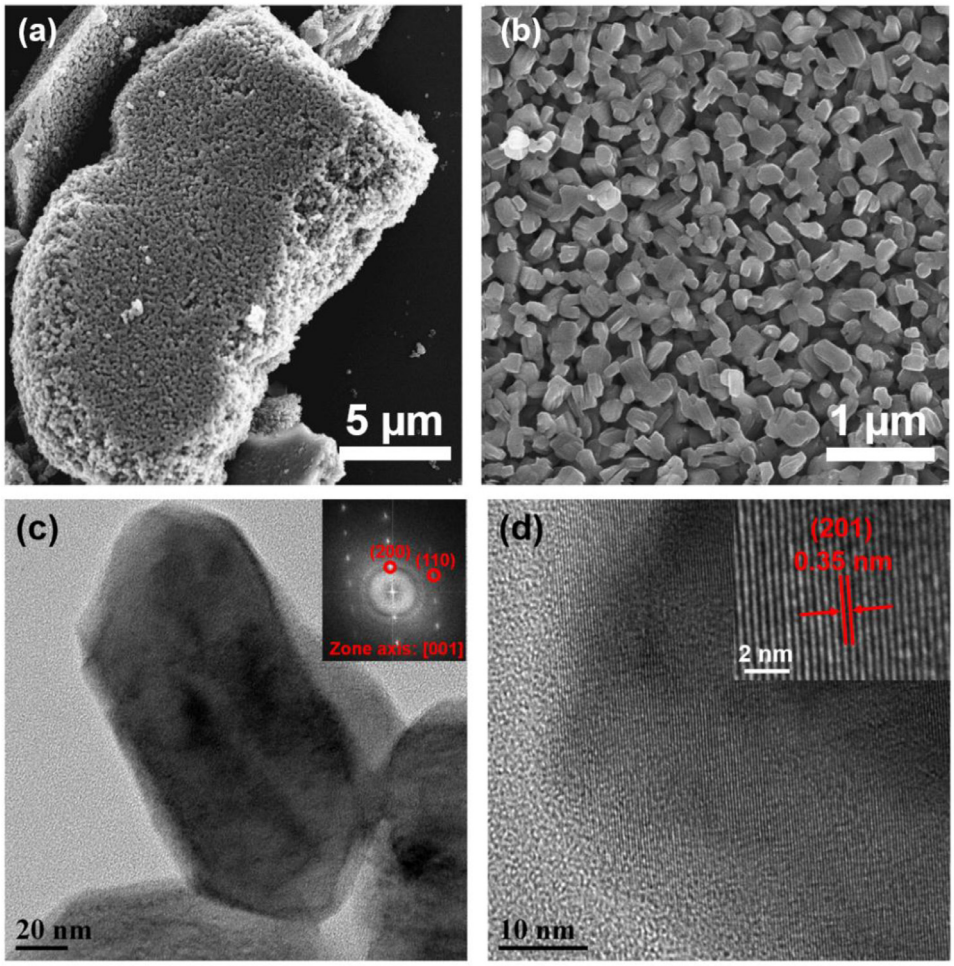

Fig. 2. (a) and (b) SEM, (c) TEM, and (d) HRTEM images of the 3D-V_2O_5 (inset in (c): SAED pattern; inset in (d): magnified HRTEM image).

delivering discharge capacities of 267, 265 and 263 mAh g^{-1} during the 1st, 2nd and 3rd cycle, respectively. Fig. 3(b) displays its cycling performance at 0.5 C. The discharge capacity slightly decays during the first ten cycles and becomes relatively stable in the subsequent cycles, which is found to be 248 mAh g^{-1} during the 50th cycle, corresponding to a capacity retention of 93%. In contrast, as shown in Figs. 3(b) and S5, the bulk V_2O_5 exhibits a large polarization, presenting lower capacities (171 mAh g^{-1} during the 50th cycle) and quicker capacity fading (capacity retention: 76%). Moreover, the cycling stability of the 3D-V_2O_5 is also much better than the previously reported V_2O_5 cathodes, e.g., 85% capacity retention for reduced graphene oxide supported porous V_2O_5 spheres at 0.3 C after 50 cycles [34], 79% capacity retention for porous V_2O_5 yolk-shell microspheres at ~0.2 C after 50 cycles [40], and 60% capacity retention for honeycomblike V_2O_5/carbon nanotube networks at ~0.3 C after 50 cycles [24].

The rate capabilities of 3D-V_2O_5 and bulk V_2O_5 at current densities ranging from 0.29 A g^{-1} (1 C) to 5.88 A g^{-1} (20 C) are displayed in Figs. 3(c) and S6. The 3D-V_2O_5 cathode exhibits average discharge capacities of 248, 230, 207, 189 and 180 mAh g^{-1} at rates of 1, 2, 5, 8 and 10 C, respectively. Even at very high rates of 15 and 20 C, the voltage plateaus are still clearly discernible (Fig. S6) and satisfactory capacities of 154 and 127 mAh g^{-1} can be obtained, respectively. Moreover, an average discharge capacity can be recovered to 247 mAh g^{-1} after various C rates discharge and charge processes, indicating the good reversibility of the redox

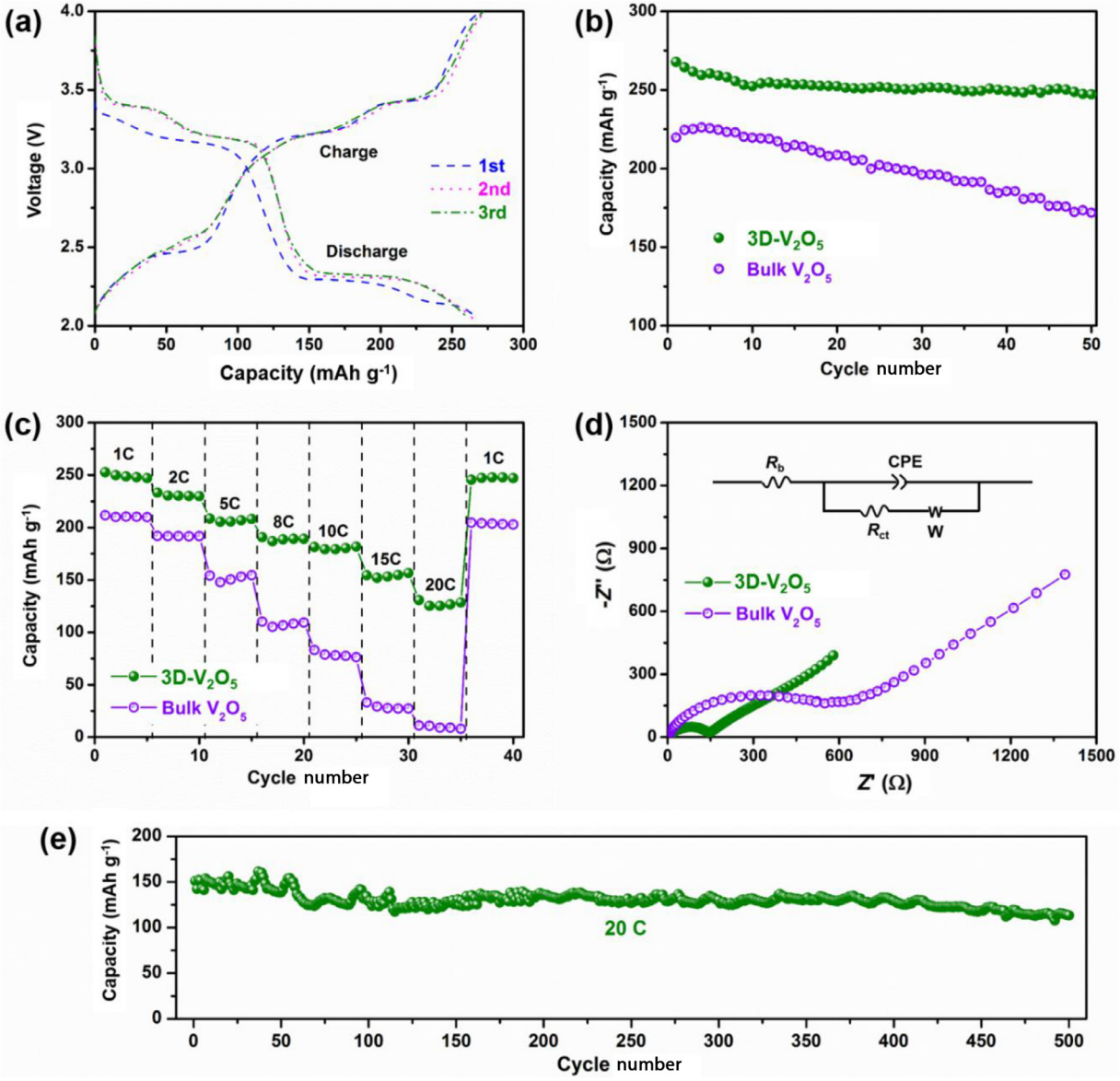

Fig. 3. Electrochemical properties of the 3D-V_2O_5 and bulk V_2O_5. (a) Charge-discharge profiles of the 3D-V_2O_5 at 0.5 C. (b) Cycling performance at 0.5 C. (c) Rate capability. (d) EIS and corresponding fitted equivalent circuit model (inset). (e) Long-term cycle life of the 3D-V_2O_5 for 500 cycles at 20 C.

reactions. In a comparative study, the bulk V_2O_5 shows lower capacities of 210, 191, 153, 107 and 78 mAh g^{-1} at rates of 1, 2, 5, 8 and 10 C, respectively, and has almost no electrochemical responses at higher rates of 15 and 20 C. To elucidate the kinetics of the electrochemical reactions on the 3D-V_2O_5 electrode, electrochemical impedance spectroscopy (EIS) measurements were carried out on the cell at the third fully charged state (Fig. 3(d)). The semicircle in high-frequency region represents the charge transfer resistance (R_{ct}) between 1 M $LiPF_6$ in EC/DMC (1/1, w/w) electrolyte and the V_2O_5 cathode, while the sloping line in low-frequency region stands for the Warburg resistance that corresponds to Li^+ diffusion in the V_2O_5 cathode. Thus, an equivalent circuit (inset in Fig. 3(d)) was built to explain the above EIS study. It is found that the R_{ct} for the 3D-V_2O_5 is 136 Ω, while that for the bulk V_2O_5 is as high as 670 Ω, implying faster charge-transfer kinetics for the 3D-V_2O_5. Moreover, the C-rate performance of the 3D-V_2O_5 is also excellent as compared to the state-of-art V_2O_5 cathodes, e.g., hierarchical sisal-like V_2O_5 (105 mAh g^{-1} at 10 C) [41], V_2O_5 hollow microspheres (~60 mAh g^{-1} at 10 C) [42], yolk-shell V_2O_5 sub-microspheres (87 mAh g^{-1} at 12 C) [43], carbon nanotube modified V_2O_5 porous microspheres (109 mAh g^{-1} at 10 C) [44], and graphene/V_2O_5 cryogel composite (~100 mAh g^{-1} at 10 C) [45]. To further demonstrate the advantages of the 3D-V_2O_5, its cycle life at a high rate of 20 C was investigated (Figs. 3(e) and S7). In the initial stage, the discharge capacity is around 150 mAh g^{-1}, and remarkably, a capacity of 115 mAh g^{-1} is still obtained after 500 cycles (capacity retention: 77%), which passes beyond many V_2O_5 cathodes, e.g., V_2O_5 hollow microspheres (~112 mAh g^{-1} at 10 C after 500 cycles) [46], monolithic interwoven V_2O_5 nanobelts/carbon nanotubes architectures (~113 mAh g^{-1} at 6.8 C after 500 cycles) [47], demonstrating an outstanding high-rate and long-term cycling performance.

To understand the greatly improved lithium storage properties of the 3D-V_2O_5, the electrode kinetics was studied in details using cyclic voltammetry (CV) technique. Fig. 4(a) and (b) shows the CV curves of the 3D-V_2O_5 and bulk V_2O_5 at different scanning rates (0.1, 0.2, 0.3 and 0.4 mV s^{-1}). Several obvious pairs of redox peaks are consistent well with the voltage plateaus in discharge-charge

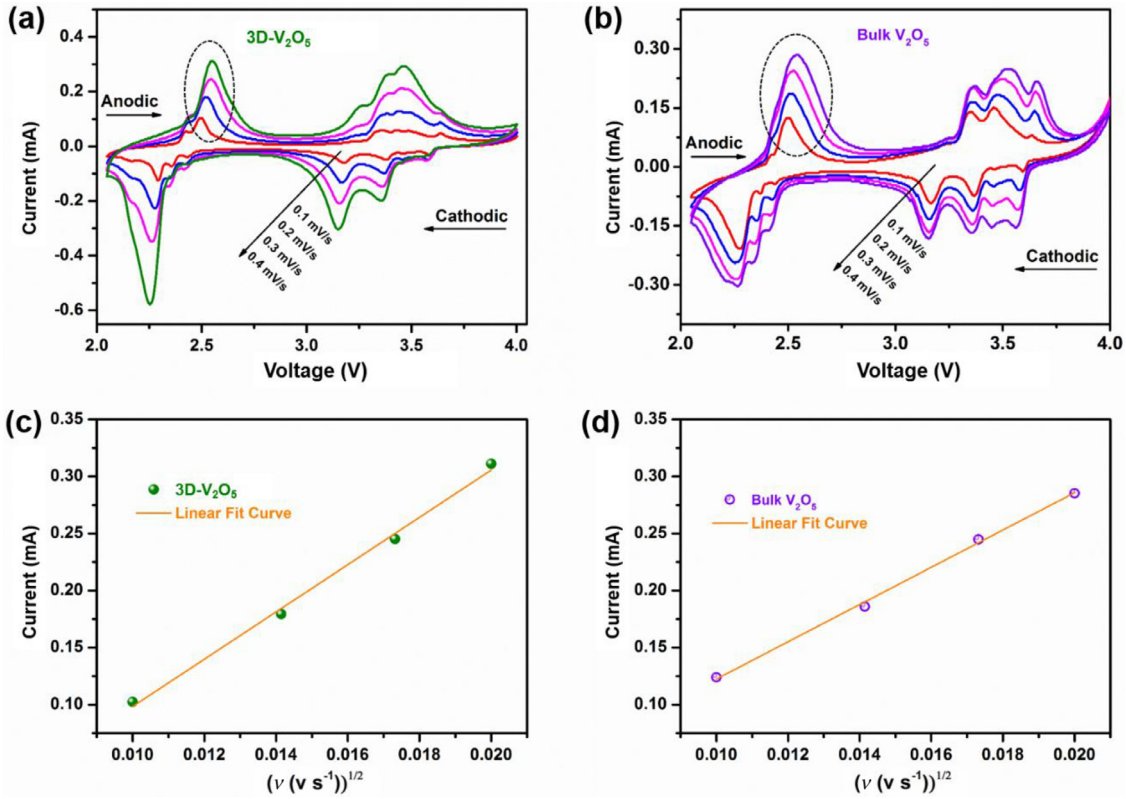

Fig. 4. CV curves of the (a) 3D-V_2O_5 and (b) bulk V_2O_5 evaluated at various scan rates, and (c) and (d) the relationship of the current of the oxidation peak marked by a circle in (a) and (b) and the square root of scan rate.

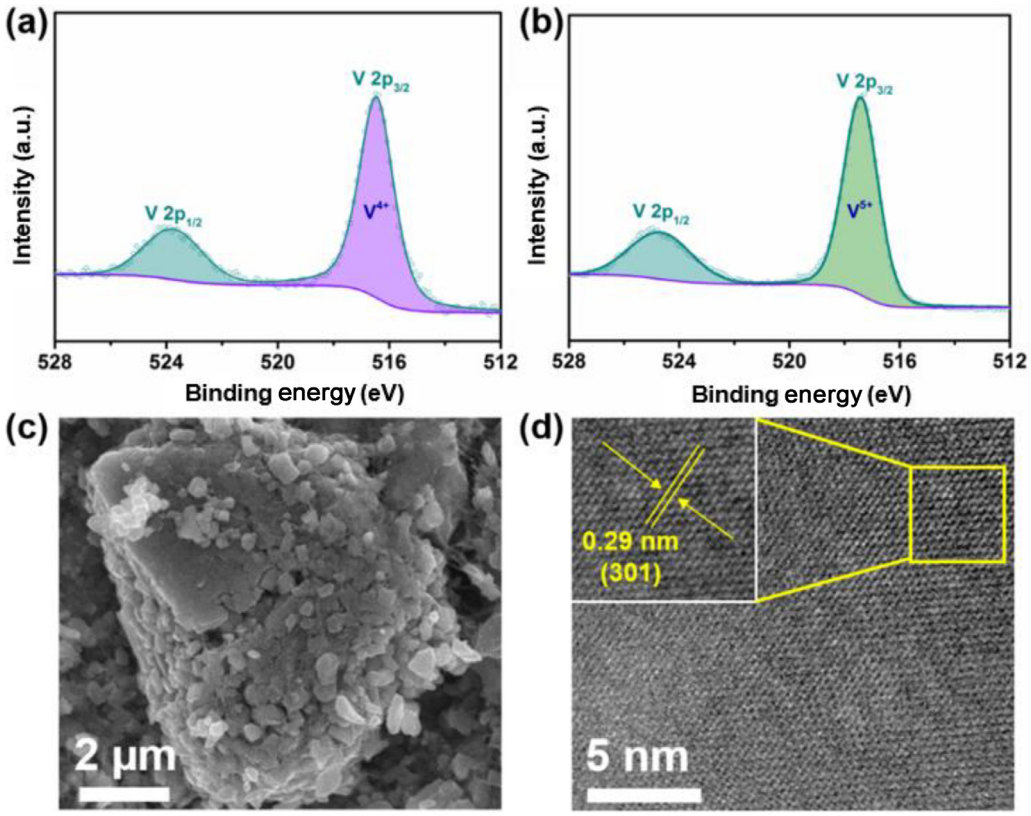

Fig. 5. The high resolution XPS spectra of the V 2*p* region in 3D-V_2O_5 cathode examined at the first discharge (a) and charge (b) states. (c) SEM and (d) HRTEM images of the 3D-V_2O_5 cathode after long-term cycle (500 cycles at 20 C).

curves (Fig. 3(a)). Oxidation peaks at around 2.5 V (marked by a circle in Fig. 4(a) and (b)) were selected as an example to analyze the apparent chemical diffusion coefficient of Li-ions ($D_{(Li^+)}$). As shown in Fig. 4 (c) and (d), the peak current (i_P) exhibited a linear relationship with the square root of the scan rate ($v^{1/2}$), indicating a typical diffusion-controlled process [48]. Then, D_{Li^+} can be determined by the following Eq. (1):

$$i_p = \left(2.65 \times 10^5\right) n^{3/2} S D_{Li^+}^{1/2} C_{Li^+} v^{1/2} \quad (1)$$

where n represents the charge-transfer number, S represents the contact area between electrode and electrolyte, and C_{Li^+} represents the concentration of Li^+ in the V_2O_5 cathodes. Based on the slope values in Fig. 4(c) and (d), the C_{Li^+} is calculated to be 6.2×10^{-13} and 3.2×10^{-13} $cm^2\ s^{-1}$ for the 3D-V_2O_5 and bulk V_2O_5, respectively. It is clear that the 3D-V_2O_5 evinces a faster Li-ion diffusion rate, which has mainly benefited from its highly porous architecture that ensures efficient electrolyte transportation and the interfacial contact between the electroactive nanorods and the electrolyte as well as the 3D framework that facilitates more efficient Li^+ transport across the entire electrode.

Additionally, to shed more light on the reaction mechanisms of high-rate lithium storage in 3D-V_2O_5, some ex-situ characterizations were carried out. Figs. S8 and 5(a) and (b) exhibit the X-ray photoelectron spectroscopy (XPS) analysis of the 3D-V_2O_5 at different states. As seen from the high resolution XPS spectrum of the V 2*p* region at the first discharge state (Fig. 5(a)), the peak was fitted almost entirely to V^{4+} signal ($2p_{3/2}$: 516.5 eV), which corresponds to the formation of Li-intercalated $Li_2V_2O_5$. When the cathode was charged to 4.0 V (Fig. 5(b)), the V^{4+} signal disappears and completely converts to pristine V^{5+} ($2p_{3/2}$: 517.4 eV), demonstrating the outstanding lithium storage reversibility of 3D-V_2O_5. Moreover, post-mortem SEM and HRTEM examination of the cycled 3D-V_2O_5 cathode (Figs. 5(c) and (d), S9 and S10) indicates that the 3D porous architecture and the crystallinity of V_2O_5 can be well maintained after a long-term cycling (500 cycles at 20 C), implying the perfect accommodation of the strain and volume variation during the repeated (de)lithiation processes.

4. Conclusions

In summary, a facile and environmental-friendly method was developed to prepare 3D-V_2O_5 in large-scale. This paper also highlights the feasibility of this novel electrode material to be transferred into real practice through the aforementioned synthesis method. In this synthesis, oxalic acid serves dual roles, which is responsible for the reduction of vanadium ions and the formation of porous architecture by releasing of CO_2 gas during the annealing process. The 3D porous structure provides continuous mass transportation with a reduced diffusion barrier and interconnected Li^+ transport network, thus results in enhanced lithium storage properties. A series of electrochemical measurements demonstrates the viability of the 3D-V_2O_5 as high-performance cathode for LIBs. For examples, discharge capacity of 248 mAh g^{-1} is retained after 50 cycles at 0.5 C, corresponding to a capacity retention of 93%. Even at very high rates of 15 and 20 C, satisfactory capacities of 154 and 127 mAh g^{-1} can still be obtained, respectively. The electrochemical performances of the 3D-V_2O_5 surpass the conventional bulk V_2O_5, which is attributed to the significant enhancement in charge transfer kinetics and Li-ion diffusion rate. While these results position the 3D-V_2O_5 as the prospective commercial cathode, it more generally holds significance in the context of materials design for advanced LIBs.

Acknowledgments

The authors gratefully acknowledge the National Key R&D Research Program of China (No. 2018YFB0905400), the National Natural Science Foundation of China (Grant Nos. 51622210, 51872277, 21606003 and 51802044), the DNL cooperation Fund, CAS (DNL180310), the Fundamental Research Funds for the Central Universities (WK3430000004), and Opening Projects of CAS Key Laboratory of Materials for Energy Conversion and State Key Laboratory of Vanadium and Titanium Resources Comprehensive Utilization.

Supplementary material

Supplementary material associated with this article can be found, in the online version, at doi:10.1016/j.jechem.2019.02.010.

References

[1] H. Tan, L. Xu, H. Geng, X. Rui, C. Li, S. Huang, Small 14 (2018) 1800567.
[2] Y. Tang, Y. Zhang, O.I. Malyi, N. Bucher, H. Xia, S. Xi, Z. Zhu, Z. Lv, W. Li, J. Wei, M. Srinivasan, A. Borgna, M. Antonietti, Y. Du, X. Chen, Adv. Mater. 30 (2018) 1802200.
[3] Y. Tang, J. Deng, W. Li, O.I. Malyi, Y. Zhang, X. Zhou, S. Pan, J. Wei, Y. Cai, Z. Chen, X. Chen, Adv. Mater. 29 (2017) 1701828.
[4] D. Bin, Y. Wen, Y. Wang, Y. Xia, J. Energy Chem. 27 (2018) 1521–1535.
[5] J.D. Liu, J.J. Liang, C.Y. Wang, J.M. Ma, J. Energy Chem. 33 (2019) 160–166.
[6] Y. Tang, Y. Zhang, X. Rui, D. Qi, Y. Luo, W.R. Leow, S. Chen, J. Guo, J. Wei, W. Li, J. Deng, Y. Lai, B. Ma, X. Chen, Adv. Mater. 28 (2016) 1567–1576.
[7] L. Wang, J. Sun, R. Song, S. Yang, H. Song, Adv. Energy Mater. 6 (2016) 1502067.
[8] Y. Zhang, O.I. Malyi, Y. Tang, J. Wei, Z. Zhu, H. Xia, W. Li, J. Guo, X. Zhou, Z. Chen, C. Persson, X. Chen, Angew. Chem. Int. Ed. 56 (2017) 14847–14852.
[9] Z. Zhu, Y. Tang, Z. Lv, J. Wei, Y. Zhang, R. Wang, W. Zhang, H. Xia, M. Ge, X. Chen, Angew. Chem. Int. Ed. 57 (2018) 3656–3660.
[10] Y. Wang, G. Cao, Adv. Mater. 20 (2008) 2251–2269.
[11] J. Yao, Y. Li, R.C. Massé, E. Uchaker, G. Cao, Energy Storage Mater. 11 (2018) 205–259.
[12] Y. Yue, H. Liang, Adv. Energy Mater. 7 (2017) 1602545.
[13] H.T. Tan, X. Rui, W. Sun, Q. Yan, T.M. Lim, Nanoscale 7 (2015) 14595–14607.
[14] X. Huang, X. Rui, H.H. Hng, Q. Yan, Part. Part. Syst. Charact. 32 (2015) 276–294.
[15] M. Liu, B. Su, Y. Tang, X. Jiang, A. Yu, Adv. Energy Mater. 7 (2017) 1700885.
[16] N. Aliahmad, Y. Liu, J. Xie, M. Agarwal, ACS Appl. Mater. Interface 10 (2018) 16490–16499.
[17] R. Xiao, J. Xie, T. Luo, L. Huang, Y. Zhou, D. Yu, C. Chen, Y. Liu, J. Phys. Chem. C 122 (2018) 1513–1521.
[18] J. Ding, Z. Du, L. Gu, B. Li, L. Wang, S. Wang, Y. Gong, S. Yang, Adv. Mater. 30 (2018) 1800762.
[19] Y. Wang, Z. Nie, A. Pan, Y. Zhang, X. Kong, T. Zhu, S. Liang, G. Cao, J. Mater. Chem. A 6 (2018) 6792–6799.
[20] P. Liu, K. Zhu, Y. Gao, H. Luo, L. Lu, Adv. Energy Mater. 7 (2017) 1700547.
[21] S. Fleischmann, D. Leistenschneider, V. Lemkova, B. Kruener, M. Zeiger, L. Borchardt, V. Presser, Chem. Mater. 29 (2017) 8653–8662.
[22] C. Zhang, S.-H. Park, S.E. O'Brien, A. Seral-Ascaso, M. Liang, D. Hanlon, D. Krishnan, A. Crossley, N. McEvoy, J.N. Coleman, V. Nicolosi, Nano Energy 39 (2017) 151–161.
[23] H. Yu, J. Yang, H. Fan, Crystengcomm 19 (2017) 716–721.
[24] X. Yao, G. Guo, P.-Z. Li, Z.-Z. Luo, Q. Yan, Y. Zhao, ACS Appl. Mater. Interface 9 (2017) 42438–42443.
[25] K. Palanisamy, J.H. Um, M. Jeong, W.-S. Yoon, Sci. Rep., 6 (2016) 31275.
[26] K. Lu, J. Xu, J. Zhang, B. Song, H. Ma, ACS Appl. Mater. Interface 8 (2016) 17402–17408.
[27] Y. Tang, Y. Zhang, W. Li, B. Ma, X. Chen, Chem. Soc. Rev. 44 (2015) 5926–5940.
[28] B. Yan, X. Li, Z. Bai, Y. Zhao, L. Dong, X. Song, D. Li, C. Langford, X. Sun, Nano Energy 24 (2016) 32–44.
[29] K. Shen, J. Ding, S. Yang, Adv. Energy Mater. 8 (2018) 1800408.
[30] J.S. Sakamoto, B. Dunn, J. Mater. Chem. 12 (2002) 2859–2861.
[31] H. Yan, S. Sokolov, J.C. Lytle, A. Stein, F. Zhang, W.H. Smyrl, J. Electrochem. Soc. 150 (2003) A1102–A1107.
[32] Z. Cao, B. Wei, Nano Energy 2 (2013) 481–490.
[33] C. Zhang, Z. Chen, Z. Guo, X.W. Lou, Energy Environ. Sci. 6 (2013) 974–978.
[34] X. Rui, J. Zhu, D. Sim, C. Xu, Y. Zeng, H.H. Hng, T.M. Lim, Q. Yan, Nanoscale 3 (2011) 4752–4758.
[35] Q. An, P. Zhang, F. Xiong, Q. Wei, J. Sheng, Q. Wang, L. Mai, Nano Res. 8 (2015) 481–490.
[36] Y. Zhou, X. Rui, W. Sun, Z. Xu, Y. Zhou, W.J. Ng, Q. Yan, E. Fong, ACS Nano 9 (2015) 4628–4635.
[37] L. Mai, Q. An, Q. Wei, J. Fei, P. Zhang, X. Xu, Y. Zhao, M. Yan, W. Wen, L. Xu, Small 10 (2014) 3032–3037.
[38] L.-L. Xing, G.-G. Zhao, K.-J. Huang, X. Wu, Dalton Trans. 47 (2018) 2256–2265.
[39] C. Niu, X. Liu, J. Meng, L. Xu, M. Yana, X. Wang, G. Zhang, Z. Liu, X. Xu, L. Mai, Nano Energy 27 (2016) 147–156.
[40] Y. Dou, X. Liang, G. Gao, G. Wu, J. Alloys Compd. 735 (2018) 109–116.
[41] N. Wu, W. Du, G. Liu, Z. Zhou, H.-R. Fu, Q. Tang, X. Liu, Y.-B. He, ACS Appl. Mater. Interface 9 (2017) 43681–43687.
[42] K. Kim, M.-J. Lee, Electrochim. Acta 258 (2017) 942–950.

[43] Y. Ma, A. Huang, H. Zhou, S. Ji, S. Zhang, R. Li, H. Yao, X. Cao, P. Jin, J. Mater. Chem. A 5 (2017) 6522–6531.
[44] Q. Li, Y. Chen, J. He, F. Fu, F. Qi, J. Lin, W. Zhang, Energy Technol. 5 (2017) 665–669.
[45] F. Maroni, A. Birrozzi, G. Carbonari, F. Croce, R. Tossici, S. Passerini, F. Nobili, Chemelectrochem 4 (2017) 613–619.
[46] L. Zeng, A. Pan, S. Liang, J. Wang, G. Cao, Sci. China Mater. 59 (2016) 567–573.
[47] H. Yang, G. Xu, X. Wei, J. Cao, L. Yang, P.K. Chu, J. Power Sources 395 (2018) 295–304.
[48] X. Rui, D. Sim, C. Xu, W. Liu, H. Tan, K. Wong, H.H. Hng, T.M. Lim, Q. Yan, RSC Adv. 2 (2012) 1174–1180.